

Advances in additive manufacturing process simulation: Residual stresses and distortion predictions in complex metallic components

Xu Song ^{a,*}, Stefanie Feih ^{b,*}, Wei Zhai ^c, Chen-Nan Sun ^b, Feng Li ^d, Raj Maiti ^d, Jun Wei ^b, Yangzhan Yang ^e, Victor Oancea ^e, Leon Romano Brandt ^f, Alexander M. Korsunsky ^f

^a Department of Mechanical and Automation Engineering, Chinese University of Hong Kong, Shatin, Hong Kong, China

^b Singapore Institute of Manufacturing Technology, A*STAR (Agency for Science, Technology and Research), 73 Nanyang Drive, 637662, Singapore

^c Department of Mechanical Engineering, National University of Singapore, 117575, Singapore

^d Central Technology Group, Rolls-Royce Singapore Pte Ltd, 1 Seletar Aerospace Crescent, 797565, Singapore

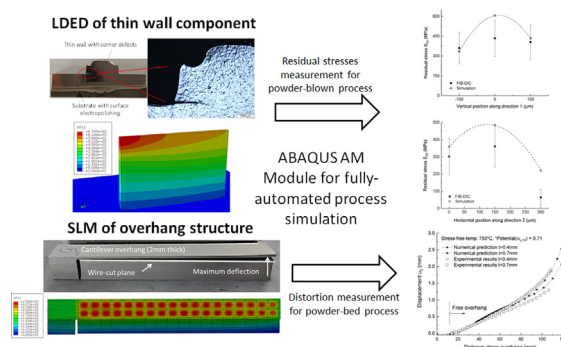
^e Dassault Systèmes Simulia Corporation, 1301 Atwood Avenue, Johnston, RI 02919, USA

^f Department of Engineering Science, University of Oxford, Oxford OX1 3PJ, UK

HIGHLIGHTS

- A computationally-efficient simulation framework is validated via residual stress and distortion measurements.
- Separate time and spatial information for material deposition and heat input need to be provided via separate event series.
- The main cause for cracking of thin-walled Inconel 718 structures is a high through-thickness residual stress at corners.
- Simulation of surrounding powder bed is important to accurately predict temperature history for complex support geometries.
- Predicted distortions of Inconel 718 cantilever structures were found to be highly sensitive to material anisotropy.

GRAPHICAL ABSTRACT



ARTICLE INFO

Article history:

Received 30 January 2020

Received in revised form 30 March 2020

Accepted 2 May 2020

Available online 5 May 2020

Keywords:

Additive manufacturing (AM)

Laser Direct Energy Deposition (LDED)

Selective Laser Melting (SLM)

Finite element analysis (FEA)

ABSTRACT

Due to rapid solidification of melted powders in metal additive manufacturing processes and high thermal gradients, large residual stresses are created in the build. This can lead to undesired distortions as well as crack initiation. The main aim of this work is to optimize the Additive Manufacturing (AM) process parameters by finite element modelling of the entire process to minimize the resulting residual stresses and distortions. We focus on two most important metal AM processes: (a) Laser Direct Energy Deposition (LDED) and (b) Selective Laser Melting (SLM). The ABAQUS AM module is employed to simulate both processes as it provides an automated interface allowing the user to define event data, such as element activation and heat input, as a function of both position and time to achieve process simulation of complex 3D parts. For the LDED processes, thin wall components are simulated, and residual stresses predictions are compared with both FIB-DIC and XRD measurement results at different scales. For the SLM process, overhanging

* Corresponding authors.

E-mail addresses: xsong@mae.cuhk.edu.hk (X. Song), feihs@simtech.a-star.edu.sg (S. Feih).



structures with different support thicknesses are simulated and compared with experimental part distortion after support removal. It is shown that the support thickness together with selected process and material properties play a key role in resulting distortions.

© 2020 The Authors. Published by Elsevier Ltd. This is an open access article under the CC BY license (<http://creativecommons.org/licenses/by/4.0/>).

1. Introduction

Over the last decade, Additive manufacturing (AM) technology has been established as a viable and cost-effective alternative to traditional subtractive metallic manufacturing processes, resulting in innovative design opportunities for complex parts. Among the large number of AM-classified processes [1], Laser Direct Energy Deposition (LDED) and powder-bed based processes, such as Selective Laser Melting (SLM), are considered the most important and dominant metal additive manufacturing techniques currently available in the market [2,3].

Due to the rapid solidification of melted metal powders and high thermal gradients of non-uniform surface heating in the metal AM processes, significant residual stresses are created within the part as well as the build platform [4–6]. As a result, these stresses lead to distortions of the build part and possibly crack initiation, propagation and complete failure during printing, if their magnitudes are above the yield strength or tensile strength, respectively [7]. In order to avoid costly trial-and-error approaches to achieve successful part printing, it is important to investigate and quantify the level of residual stresses during and after the additive manufacturing process for full scale and complex 3D components.

Post-AM residual stress measurements are relatively easy to execute and have been widely conducted during the last decade using various techniques, such as crack compliance [4], synchrotron X-ray diffraction [8] and neutron diffraction [9]. In-situ residual stress measurement during the printing process is an emerging field of research [10], but faces significant technical challenges and practicality issues, such as the requirement for custom-built processing chambers [10]. Therefore, as an alternative, numerical simulation of the entire AM process to capture the residual stress evolution during printing has become an important topic for the AM research community.

Simulation of complex 3D structures during build is computationally time-consuming and costly. Finite element analysis is generally identified as the preferred numerical method due to its ability to handle non-linear problems [2]. Commercial finite element-based software packages have recently released AM modules or provide in-built functionalities capable of simulating various approaches of thermo-mechanical analysis to predict printed part microstructure, stresses and distortions via (1) detailed Goldak or Gauss-type heat source definition with microscale resolution [11–13], (2) adaptive meshing approaches in heat source vicinity [14,15], (3) multi-scale modelling with micro-scale results imported at lower mesh resolution for 3D complex geometries [16,17] and (4) superlayer or block-dump approaches for material deposition with singular moving point nodal surface heat flux representation [18], here listed in order of decreasing computational effort. With increasing simulation simplification, computational running times reduce to times comparable to the timescale of the actual printing process, hence making AM process simulation of complex engineering components possible.

Validation of these simplified approaches remains an on-going field of research, with many research groups comparing the numerical efficiency and accuracy with results obtained with finer mesh resolution. Detailed studies of complex geometry simulation with experimental validation remain scarce, and only limited insights into the relative importance of various analysis details and input parameters exist. This is further complicated by the fact that a wide range of materials and processes exist for additive manufacturing, each with their own unique characteristics and modelling strategies. It is therefore generally unclear

to what extent simulation simplifications, the simulation set-up and specific material properties influence the residual stress and distortion results.

In the current study, we investigate process simulation of AM components printed with Inconel 718 by utilizing the AM modules incorporated in Abaqus Simulia software [18,19]. The in-built approach is able to simulate the full component AM process by introducing the concept of event series to automate element activation during the printing process. In this work, we study both LDED (Fig. 1(a)) and SLM (Fig. 1(b)) processes. Typical sample geometries such as thin wall structures for LDED and overhanging structures for SLM were designed, printed and studied. Post-AM residual stresses and distortions were measured to validate the numerical predictions. The results show that the automated AM module is a valuable tool for analyzing the influence of geometry, material properties and process parameters on distortion and residual stresses. Simulation guidelines for both processes in terms of important material properties and analysis set-up are identified in this paper.

2. Experimental details

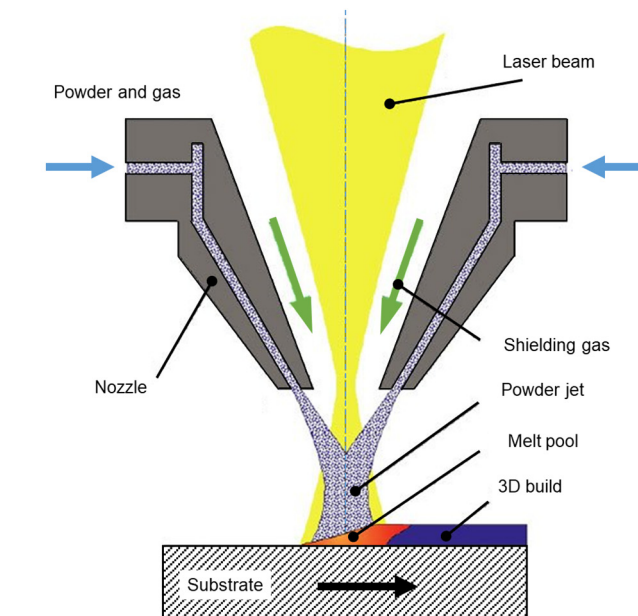
2.1. Sample geometry and process parameters for LDED

The thin-walled specimens were built using a Trumpf TruLaser Cell 7000 machine. It employs a laser source range from 50 W to 200 W for total eight layer sets with slightly different spot sizes in each set. Detailed process parameters are given in Table 1.

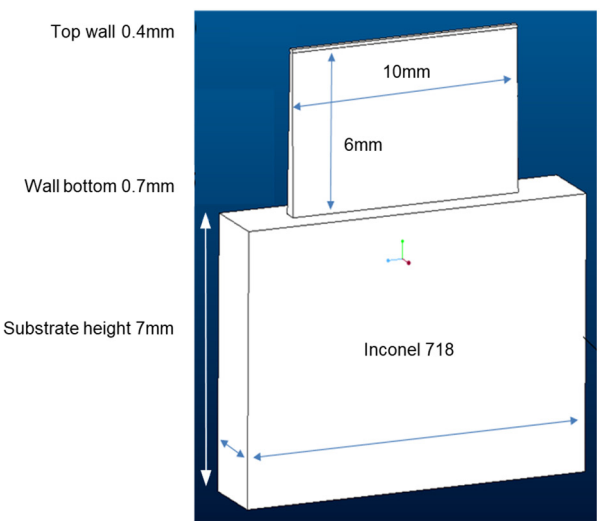
The sample geometry is planned as Fig. 2(a) with one of the actual builds illustrated in Fig. 2(b). As LDED technique is more suitable for repair work in the aerospace industry, the substrate material is selected to be the same as the top wall as Inconel 718. To demonstrate the possibility of residual stress induced cracking, a typical root crack can also be observed in Fig. 2(b) under magnification.

In order to create the tapered wall cross section as illustrated in Fig. 2(a), different LDED parameters have to be used at different built height. The optimized process parameters were determined based on company in-house studies [20] considering inter-layer bonding and built wall height control. The layer height is the actual printed dimension as we measure built height for each set. The laser energy density was calculated based on assumption of laser spot geometry of a cylinder (laser spot diameter \times layer height). The layer re-melting ratio was obtained from microstructural observations, and subsequently the laser absorption coefficient was calculated. It was then used as input for the finite element simulation (see Table 1) and agrees well with parameters used by other researchers for similar studies [14].

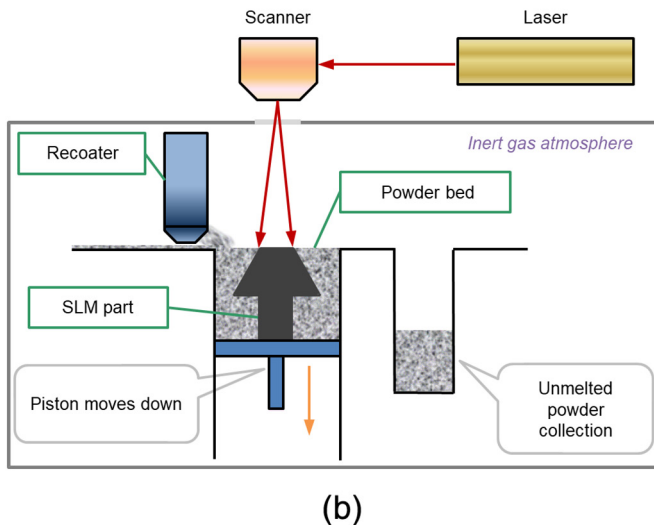
LDED samples were examined by X-ray Diffraction (XRD) for residual stress measurement using a Bruker D8 Discover machine. For XRD sample preparation, the thin wall component was firstly EDM wire cut to the near-middle section, then subjected to electrochemical polishing (ECP) to the precise middle section to remove the residual stress and finally a copper coating was introduced by EDM slitting. This work follows the procedure documented by Zhang et al. [21] with the same current density of 50 A/dm² and solution of 20 vol% sulphuric acid in absolute methanol. 55 min of ECP time was needed, as lesser time will not be sufficient to flatten the surface. After ECP, the sample is presented to the XRD machine with beam spot size 1 mm and count time of 3 s. The standard $\sin^2\psi$ method [22] was employed with peak (420) selected as the reference lattice plane.



(a)



(a)



(b)

Fig. 1. (a) Laser Direct Energy Deposition (LDED) and (b) Selective Laser Melting (SLM) processes.

2.2. Sample geometry and process parameters for SLM

Structures under investigation were fabricated using EOS certified Inconel 718 powder [23] in an EOS M400 SLM equipment under inert Argon atmosphere. The equipment uses a laser source at 300 W with an approximate scanning speed of 1000 mm/s during build. Detailed process parameters are given in Table 2. The EOS M400 machine has a platform size of 400 mm × 400 mm, representing one of the largest commercial platform sizes with single laser source at the time of its

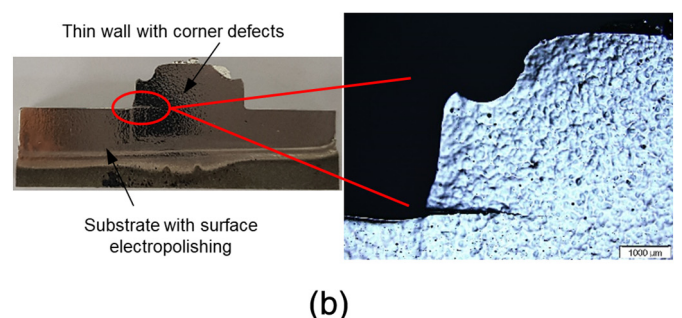


Fig. 2. (a) Dimensions of the thin wall component on the substrate and (b) actual thin wall component with magnification of the crack at the root corner for LDED process.

launch. The size of the platform influences the cooling behavior of the structure as a larger platform increases the overall recoating and hence builds time. The build process consists of three sequential steps. Firstly, the platform is lowered to achieve the right build height per layer (40 μm, see Table 1). Secondly, the powder is deposited and compacted with a rigid blade. Lastly, the laser source moves to melt the correct areas per layer. This process is repeated until the build process is completed. Energy input only occurs during the laser exposure step, which can be relatively short in comparison to the other two processes of powder layer deposition and platform movement. It is therefore important to consider the relatively long cooling process following laser heating in the event series definition in order to accurately examine the process.

The overhanging structure utilized to evaluate residual stresses and the influence of support structures is depicted in Fig. 3(a). This printed structure tends to curve upwards following wire-cutting from the support base as shown in Fig. 3(b). The maximum deflection measured is then an indicator of residual stress present during build. A lower deflection result indicates lower stresses and hence better heat management during build. Large residual stresses can lead to printing errors due to

Table 1

Build process parameter range for LDED print.

Powder type	Inconel 718	Spot size	0.18–0.6 mm	Scanning speed	20 mm/s
Particle size	20–53 μm	Power	50–200 W	Number of layer set	8
Layer thickness	80–160 μm	Platform temperature	26 °C	Number of layers in each set	6–10
Energy density	221–1229 J/mm ³	Layer re-melting ratio	28–55%	Absorption coefficient	0.28–0.45

Table 2
Build process parameters for SLM print.

Powder type	Inconel 718	Spot size	~100 μm	Scanning speed	1000 mm/s
Particle size	20–53 μm	Power	300 W	Hatch spacing	0.11 mm
Layer thickness	40 μm	Platform temperature	80 °C	Rotation angle	67°

excessive deformation during print or part cracking. Both problems add significant cost and lead time to AM printing processes.

3. Numerical models

3.1. Additive manufacturing simulation methodology

The new ABAQUS AM Module was employed in this study to simulate the complete AM process. As the simulation of the 3D printing process requires numerical interpretation in terms of automated element activation and related heat input in time and space, the ABAQUS event series module was utilized to prescribe the imposed tool path and process conditions. Once the 3D printing process is translated into event series format, the newly introduced tool path - mesh intersection module (see Fig. 4) automatically computes the relevant information required for the thermal and structural FE analysis, including the element activation and relevant thermal and structural boundary conditions for each given time step.

Build direction for the new intersection tools is defined in global z-direction. Additional built-in subroutine functions facilitate the automation of the element activation and calculation, such as a subroutine for continuous fine-scale material addition (UEPACTIVATIONVOL), which interprets the event series information for material deposition, and a subroutine for moving heat flux problems (UMDFLUX), which applies the heat input based on the respective event series information. Details of the subroutines can be found in the User's Manuals and related publications [12,13,18,19] as the above listing only covers a small portion of the new functionality.

Different AM technologies possess distinctly different features and in turn require different simulation approaches. As a result, different event series inputs have to be created for material deposition and heat input to mimic the AM printing process. For LDED processes, there are fewer

Shape	Point	Infinite Line	Box
Schematic			
Machine tool examples	Point lasers for coarse meshes	Recoater in powder-bed fabrication	Material deposition nozzle in polymer extrusion, wire-feed, laser blob for fine meshes, etc.

Fig. 4. Intersection shapes for event series interpretation in the ABAQUS AM Module. SLM processes typically utilize coarse meshes with "point" approaches to interpret the heating process and "infinite lines" for the separate process of recoater element activation. LDED processes generally use a fine mesh with "box" approaches to simultaneously deposit and heat the newly activated elements.

layers for the full build and laser parameters are generally changing with build height. Considering computational time constraints and file size restrictions, it is possible to utilize a very fine mesh to resolve each build layer for this process. The chosen intersection tool unit should then be a box (see Fig. 4), where the simultaneously applied material deposition and distributed heat flux input is described via an in-built subroutine by the generally-accepted double ellipsoidal Goldak model to describe the melt pool geometry [2,24].

For SLM processes, in contrast, each layer height is relatively small with a much larger number of total layers to be deposited and the laser process parameters usually remain constant throughout the printing process. Here, for the sake of computational efficiency and manageable file sizes, it is imperative to be able to use one element to represent multiple layers of printing. It is then important to consider that element activation during recoating and heating processes occur based at different times in the event series to account for the finite cooling time effect during the recoating event, which is typically in the order of several seconds depending on platform size. Fig. 4 shows the designed intersection tools linked to SLM processes. The recoater for the powder dispersion can be considered as an infinite line to firstly activate elements of the newly deposited layer for an adequate time interval. Thereafter, the laser spot heating source can be considered as a point for the intersection tool unit and partial or full element activation may be utilized. The heat energy due to the moving heat source is interpreted as a nodal surface heat flux for the given time increment and is assigned to the respective top surface nodes of the latest activated element layer as a function of time and location; a valid approach if the size of the heat source is small relative to the characteristic element size. For both approaches, a finite cooling time following the completed build process is also considered.

Due to the nature of the AM processes, the transient heat transfer and quasi-static stress analysis steps are commonly treated as weakly coupled under the assumption that the mechanical response during the build does not significantly alter the thermal boundary conditions [2,25], hence they are calculated in consecutive analysis steps. For the thermal analysis, heat losses occur through a combination of conduction, convection and radiation. Appropriate simulation parameters for convection and radiation to air are utilized here ($h = 18 \text{ W/m}^2\text{K}$ and $\varepsilon = 0.45$ [14,18], ambient temperature $T_{\text{amb}} = 26^\circ\text{C}$). Emerging external surfaces are important to consider for heat losses and are automatically identified and updated during the build process via the event series tools.

For the structural simulations, the build plate boundary conditions at the lower surface are set to ensure no movement. For the quasi-static stress analysis, Abaqus then calculates the thermal strain history during the 3D printing process based on the temperature difference between the defined stress-free temperature, above which thermal straining is considered to induce negligible thermal stress, and part temperature.

Temperature-dependent plasticity with the von Mises yield criterion is utilized to model the flow stress and plastic strain development during the printing process. The material properties at elevated

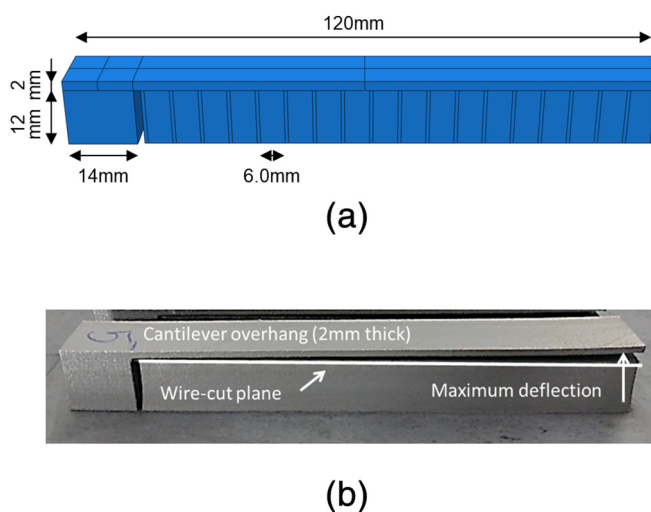


Fig. 3. (a) Overhanging cantilever designed to evaluate distortion, residual stress and microstructure for different support structures for SLM process. (b) Actual SLM build part with maximum deflection following wire-cutting below solid plate as indicated.

temperature are crucial for the correct evaluation of stresses following print. For Inconel 718, material stiffness and yield strength properties were found to be direction-dependent after the AM print process due to columnar grains growing epitaxially from one build layer to the next [23,26]. Through-thickness (z) direction properties (stiffness, strength) are generally around 15–25% lower than the respective in-plane properties for the as-built condition [23], which was also confirmed via in-house measurements. Orthotropic stiffness properties are consequently defined for the elastic response.

Temperature-dependent stress-strain curves for numerical input are visualized in Fig. 5. Properties were defined as temperature-dependent according to general alloy data for Inconel 718 provided in [27,28]. Stiffness and strength values for elevated temperatures were scaled to the room temperature values measured in-house for different build directions for the as-printed Inconel 718 SLM material. The strain-rate

hardening behavior at elevated temperatures was assumed to remain self-similar compared to room temperature measurements.

The impact of the accurate representation of anisotropic properties on resulting distortions is also assessed in this paper, and SLM distortions were found to be highly sensitive to the degree of plastic anisotropy as will be outlined in Section 4.3. The anisotropy in the yield strength envelope based on build direction was defined via Hill's potential function in the Abaqus plasticity model [19].

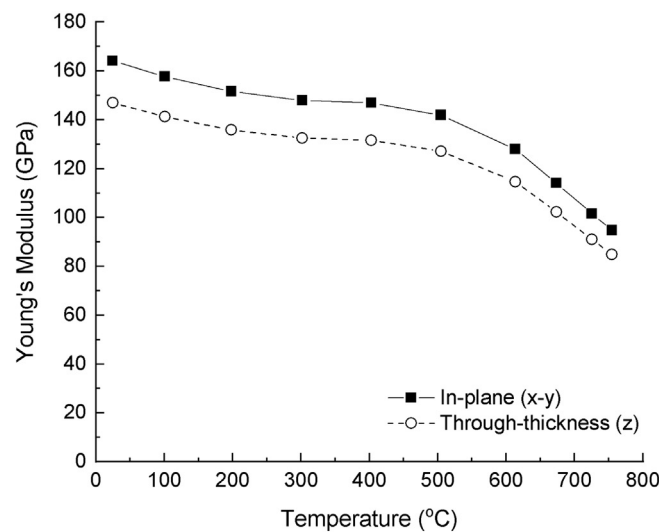
The additional strain component due to solid-state phase transformation was neglected for the simulations presented in this paper, although material-specific subroutines considering the high thermal gradients during the SLM build process can be included during the thermal analysis step and have been validated for other alloys [12,13]. This development for Inconel 718 was considered out of scope for the current paper.

Convergence of the model can require several iterations per increment, which adds significantly to the computational time required for AM simulation. For improved convergence for this highly non-linear model, strain state extrapolation for the new increment based on the previous increment result was turned off as the heating source movement results in significantly varying local strain states. Convergence was also found to improve when unsymmetric stiffness matrix storage was specified to solve the nonlinear problem with Newton's method [19].

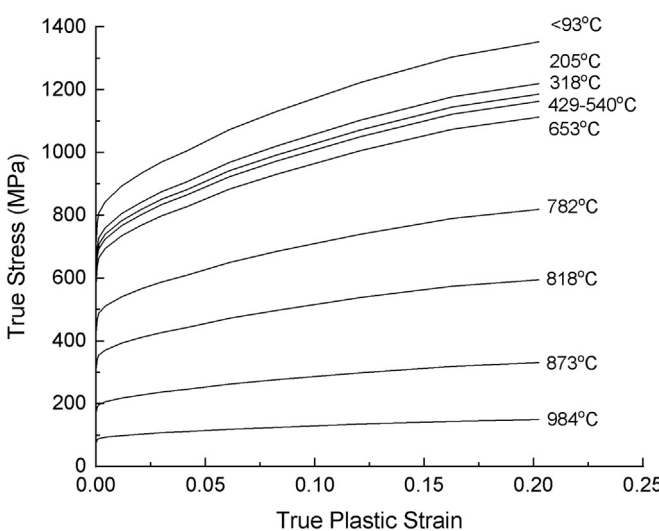
3.2. Further considerations for LDED model setup with Goldak heating

Determining model parameters for Goldak LDED input for the melt pool description (see Fig. 6) is always a challenge. In the current attempt, we fix as many variables as possible to physical parameters, namely a and c to the laser spot size, b as the layer height and Q as laser power damped by a varying absorption coefficient listed in Table 1. The processing parameters in the experiment are used as input for the Goldak model.

Preliminary mesh sensitivity studies were carried out. The converged minimum element size is 0.04 mm in height (4 elements through depth for each build layer), 0.05 mm in length and at least 4 elements in width. This resolves the heat input for the Goldak model sufficiently. Time increment was chosen as 0.0025 s to ensure that in each increment at least one element is activated. Secondly, we used tie constraints to bond the temperature and displacement degrees-of-freedom of the build part and substrate in the horizontal plane so that



(a)



(b)

Fig. 5. (a) Stiffness and (b) stress-strain responses measured at room temperature for as-printed SLM Inconel 718 tensile specimens were scaled as a function of temperature based on data reported in [27,28].

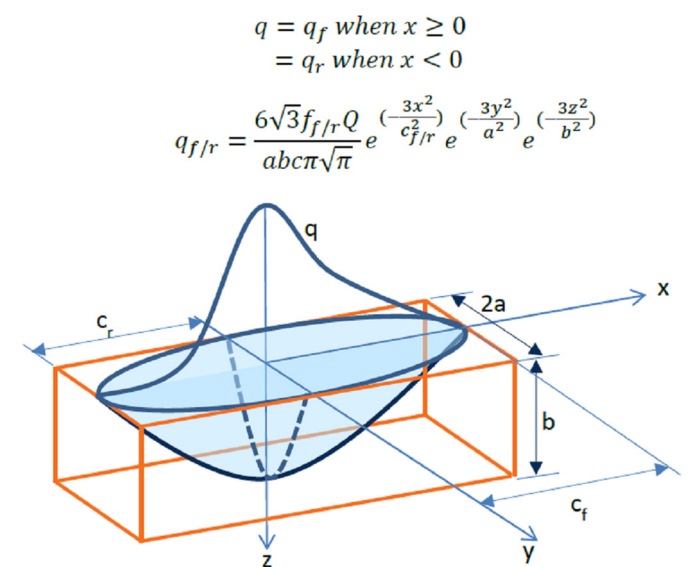


Fig. 6. Double ellipsoid Goldak model for the distributed heat flux input for LDED process.

the mesh density for the build part and base plate can be different. The model consequently had a total of 246,400 elements for the build part and 20,304 elements for the base plate. Thirdly, an additional cooling stage was added after the last step of printing, where an estimation of 100 s was applied for the cooling stage to reduce the temperature to ambient level. Fig. 7(a) illustrates the temperature profile directly following print completion with the highest temperature still predicted as ~600 °C, while Fig. 7(b) shows the temperature reduction after 100 s cooling to room temperature.

In order to change the laser parameters during LDED processing with progressing build height as typical for this type of process, several heat and stress analysis steps within a continuous time series needed to be defined to build additional layers. This allows for a progressive approach to speed up the simulation time by running heat analysis and stress steps in parallel on a multiple core machine: as we define a total of eight sets of laser parameters for the 6 mm build height, we can create eight steps for both heat transfer and stress analysis. When the heat transfer is finished for the 1st step (HT-1), its results were used to start the 1st step of stress analysis (S-1, as it requires temperature results from HT-1) while we are in parallel running HT-2.

Preliminary studies were conducted to optimize the use of respective multiple CPUs for each step to minimize the total computational time taken for the analysis using the abovementioned progressive approach. Total runtime for the model depends on both the number of available CPUs and sufficient RAM capacity to temporarily store the large model information. For our case, running with 8 CPUs, the full

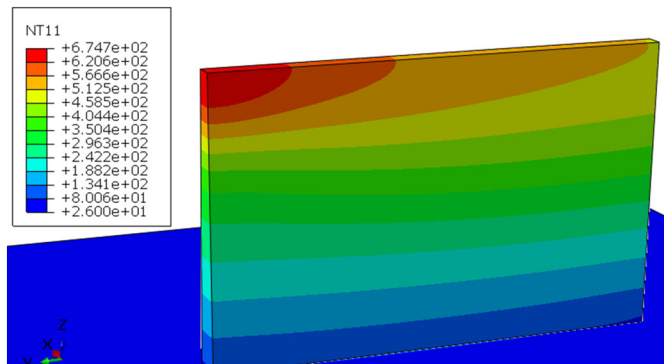
model (thermal and stress analysis) required approximately 140 h to complete.

3.3. Further considerations for SLM model setup with point heating

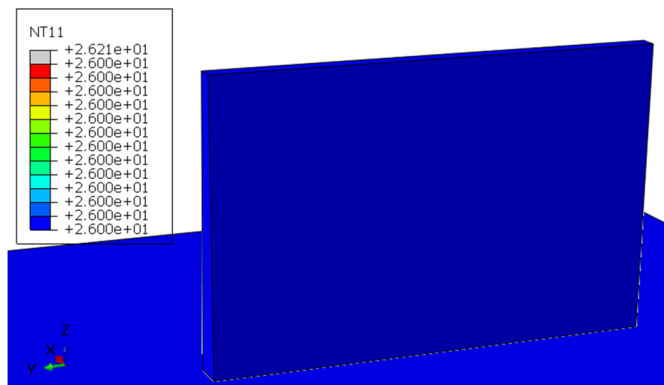
For SLM process simulation, time incrementation was set as one time increment per build layer. The total time for each build layer was calculated based on the laser path details for each layer, as well as the recoating time. An element height of 0.5 mm was chosen for the support and block structure. The overhang structure was simulated with an increased mesh density of ten elements through its thickness to capture the influence of temperature and stress gradients more accurately. The mesh is shown in Fig. 8 with ~200,000 elements used for the print part and 100,000 elements for the powder part. Full element activation [18] was utilized for both heat transfer and stress analysis. Linear heat transfer elements (DC3D8) were used for the heat transfer analysis, resulting in converged temperature results for the chosen time incrementation. Preliminary numerical studies indicated the importance of including (1) the effects of the building platform, which acts as a finite heat sink due to its preheated lower surface temperature of 80 °C, and (2) the surrounding material powder. The powder material is explicitly modelled in this work during the thermal analysis step and therefore captures the fact that the powder material within the support structure cavities acts as a finite heat sink, an effect which influences the thermal history during the build process and cannot easily be simplified. Thermal properties for Inconel 718 powder are based on particles with small contact at lower temperatures [29] and subsequent material sintering and contact zone increase at temperature above 650 °C [30]. At room temperature, the thermal conductivity of the powder was measured to be $k_p = 0.22 \text{ W/mK}$ [31].

Nodes located at the interfaces between powder and build part were equivalenced for the temperature step (see Fig. 8) to avoid the automated detection of additional free vertical surfaces during each layer activation by the in-built subroutine and generation of unrealistic heat losses during the build process originating from these internal interfaces. Adiabatic thermal boundary conditions were utilized for the longer outer surfaces for this unit cell mimicking the presence of neighboring parts during build. These thermal boundary conditions are non-critical to the temperature history given the size of the surrounding powder bed.

The powder was removed from the model following thermal analysis due to its negligible structural stiffness to speed up the analysis. The quasi-static stress analysis uses the calculated nodal temperatures from the transient heat analysis step as an interpolated input field for the solid structure, while temperature history for the powder material is ignored. Preliminary studies showed that results were comparable to



(a)



(b)

Fig. 7. (a) Temperature contour of the thin wall directly after printing; (b) Temperature contour of the thin wall after 100 s of cooling for LDED process.

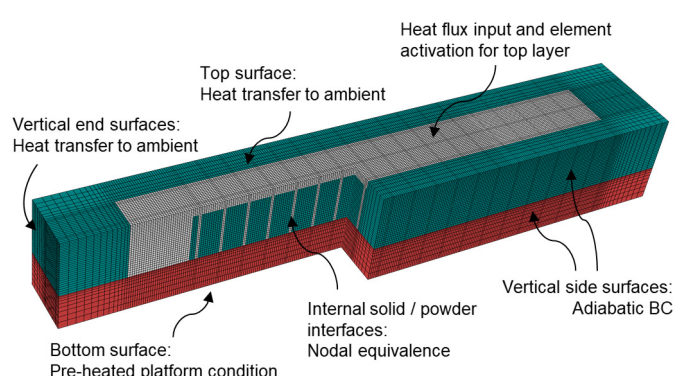


Fig. 8. SLM model set-up with build platform as unit cell approach with adiabatic surfaces. The model nodes at vertical solid-powder part interfaces are equivalenced to avoid the automated detection of emerging surfaces with unrealistic heat loss during the build process.

stress simulations including the powder material, but numerical time was reduced significantly due to the smaller model size.

Following the completed stress analysis, the support structure elements under the cantilever arm were subsequently removed via model change requests at the end of the stress analysis to visualize the resulting distortions upon wire-cutting from the support structure. Resulting distortions were found to be sensitive to element type, resulting in hourglass effects for reduced integration elements. Linear elements with full integration (C3D8) were therefore chosen for the stress analysis to capture shear and bending stresses in the overhang section of the model.

By describing the laser path accurately via an event series as a function of position and time for point-wise nodal heating, the in-build ABAQUS subroutine UMDFLUX can distinguish the heat input for the solid elements of base, overhang and support structure from the unheated surrounding powder elements. A continuous laser path was defined across the solid areas of the cantilever design with the adequate hatch spacing, and the laser power was turned off while crossing the powder-filled gaps between the base and support as well as within the hollow support structure. It is noted that this is only necessary when modelling the surrounding powder bed as a separate material. The laser path was defined via in-house coding as the exact movement of the laser source is generally a well-kept secret by the equipment manufacturer. Laser path rotations of 67° between each layer were considered. The final boundary tracing at lower laser power was also considered for each layer.

Timepoint specification was utilized to allow for customized time incrementation during laser movement. Time increments were set to a maximum of one time increment per print layer (including both heating and cooling events) or split into smaller increments capturing both heating and cooling events with separate resolution. With a use of 8 CPUs, a typical total runtime for this model with one time increment per print layer was around 6 h for the temperature analysis and approximately 24 h for the stress analysis.

4. Results and discussion

4.1. Comparison of temperature fields derived by Goldak and point heating

For initial validation studies of the new intersection modules, the point-based interaction tool for coarse meshing was benchmarked against the more classic Goldak-type approach with high mesh resolution for a cylindrical specimen on a build-plate with surrounding powder bed. Preliminary studies found that the surrounding powder bed and attached build platform significantly influenced local cooling rates in the 3D printed part and therefore needed to be considered for accurate temperature profile prediction as shown in Fig. 9. For converging

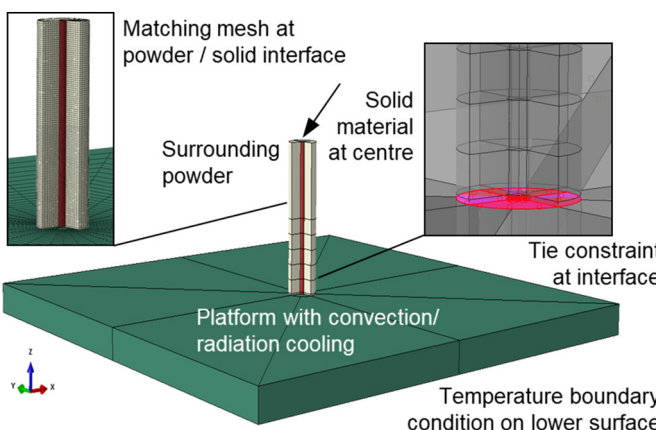
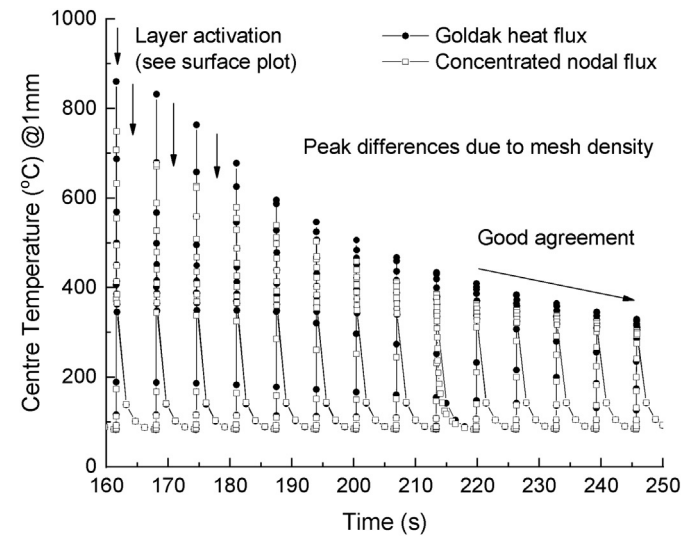


Fig. 9. Model set-up for comparison of heat source resolution influence for Goldak and point-wise nodal heating.

temperature profiles, the diameter of the surrounding powder had to be selected to be around three to five times larger than the solid part. For the Goldak melt pool modelling approach, a mesh size corresponding to one element per build layer was chosen ($\sim 40 \mu\text{m}$), while for the block-dumping approach with point heating 12 layers were merged within one element layer ($\sim 0.5 \text{ mm}$).

A laser path script was created to allow for the laser path calculation for cylindrical cross-sections as per Table 2, taking into account of hatch spacing for line distance, spot size radius for edge distance and rotation angle for subsequent build layers. The same event series were used for nodal heat distribution and Goldak melt pool simulation, as well as recoater (cooling time) definitions.

The peak temperatures determined during the build process depend on the temperature increment chosen for the laser movement step for the transient temperature analysis. For the same temperature increment (here chosen as 0.01 s), the Goldak model predicts a higher peak temperature compared to the distributed nodal heat flux model due to two reasons: (1) the Goldak model is a volumetric model, and the energy is distributed over the volume of several element layers away from the top surface and its cooling surface boundary effects; and (2) the thicker element activation layer introduces a larger surface area for



(a)

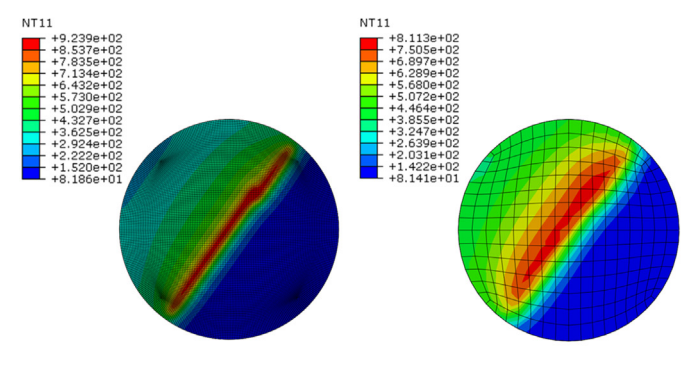


Fig. 10. (a) Peak temperature results at center point at a cylinder height of 1.0 mm and (b) surface temperature plot distribution for left: Goldak heat source and right: nodal point heat source at time $t = 169.09 \text{ s}$.

heat convection and radiation and a larger element volume for heat to conduct into due to its initial room temperature state at activation. Despite these simplifications, Fig. 10 shows the good agreement for the two approaches when comparing local temperature profiles, especially once additional laser passes are registered within the same element layer for the coarser mesh.

From these initial investigations, it is obvious that a suitable time incrementation for the Goldak approach is necessary for detailed local residual stress investigations as in the case of LDED simulations in

Section 4.2, while investigations of macroscopic deformations, such as for the SLM studies in Section 4.3, may be captured by a coarse mesh approach with point-wise heating. An adaptive meshing approach switching between the two approaches can be envisaged for future research studies.

4.2. Residual stresses in the LDED thin wall components at different scales

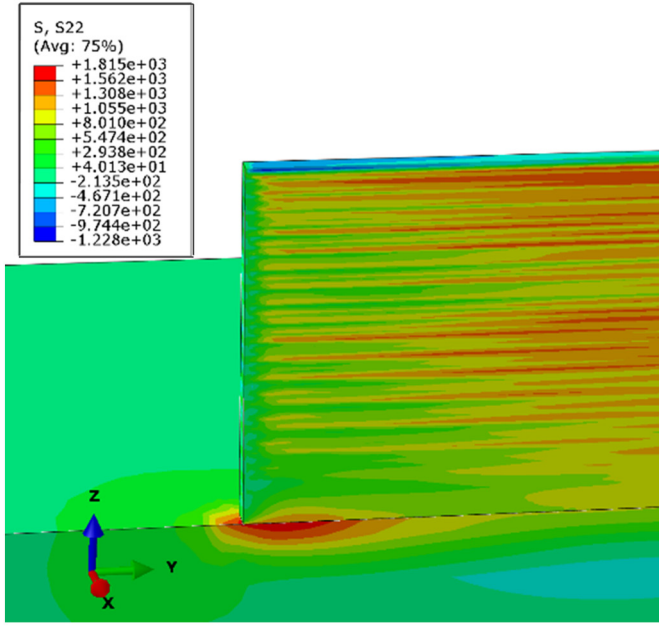
Fig. 11 illustrates the residual stresses in scanning (S_{22} , along Y-axis) and height (S_{33} , along Z-axis) direction in the thin wall component. Due to the resulting symmetric stress distributions, only the left half of the thin wall is displayed here. The highest tensile stresses exist in the lower corners of the wall at the interface between the wall and the substrate for both S_{22} and S_{33} . Similar results have also been reported by [36], especially for high residual stress value in S_{33} component. This may lead to cracking at the corners as illustrated in Fig. 2(b) and eventually premature failure of the entire work piece. This image also provides some initial qualitative validation of the model.

In order to obtain quantitative comparisons at such localized regions, a microscale residual stresses measurement technique had to be employed, in this case the Focused Ion Beam (FIB) slitting + Digital Image Correlation (DIC) imaging method [32,33]. This method allows the user to obtain the residual stresses at micron-level (usually 1–5 μm spot size) semi-destructively, ideal for micro part residual stress measurement, such as thin nitriding layers [34], single metal powder particles [35] and corner of a thin wall as in this instance (Fig. 2a).

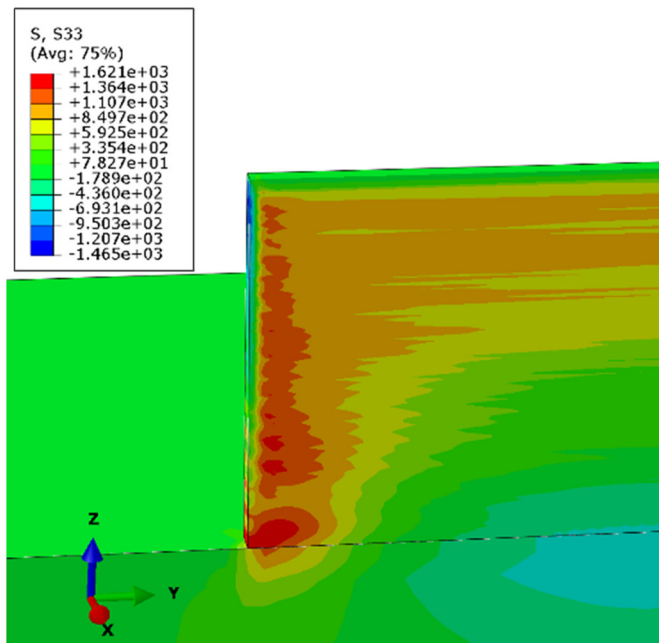
The desired ring-core pattern and their layout is illustrated in Fig. 12. Inside each ring core, the black ring region represents the circular trench, which has 0.5 μm in width and 5 μm in depth. The inner big circle region represents the “island” with a diameter of 4.5 μm . The ring cores are 150 μm apart from each other in both direction 1 (vertically) and 2 (horizontally), with Point 2 sitting on the bond-line between the thin wall and substrate, while Point 4 directly beneath the thin wall edge.

Fig. 13 summarizes the results from FIB-DIC and FE simulation at the corresponding positions (Points 1–5). We observe that the residual stresses in this region are largely tensile in nature, which was already shown in Fig. 11 and independently reported by [36]. Notice has to be taken that the tensile stress is higher at the bond line and gradually drops towards both the inner thin wall and the substrate. It is also interesting to note that the tensile stress is higher at 150 μm along the horizontal line at the substrate than that of the corner 0 μm or further down 300 μm , and this trend is captured by both the FE simulation and FIB-DIC experiment. Such detailed observation has not been reported previously due to limits of both numerical and experimental resolution. This warrants further investigation and understanding.

For the overall residual stress comparison and model validation, X-ray diffraction technique is employed. The standard $\sin^2\psi$ method, which is a built-in function of Bruker D8 Discover machine, was employed to measure the residual stresses in the cross section. Four



(a)



(b)

Fig. 11. Residual stresses in (a) S_{22} scanning direction and (b) S_{33} height direction for LDED process.

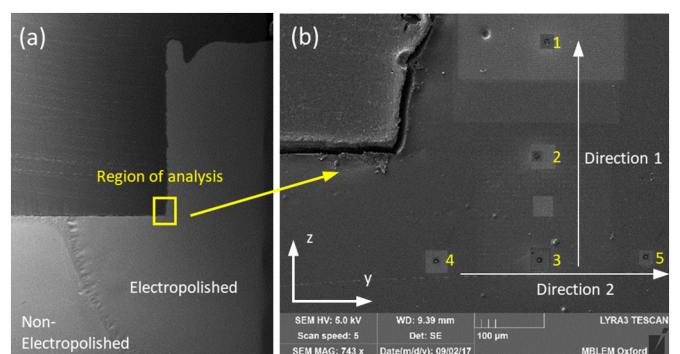
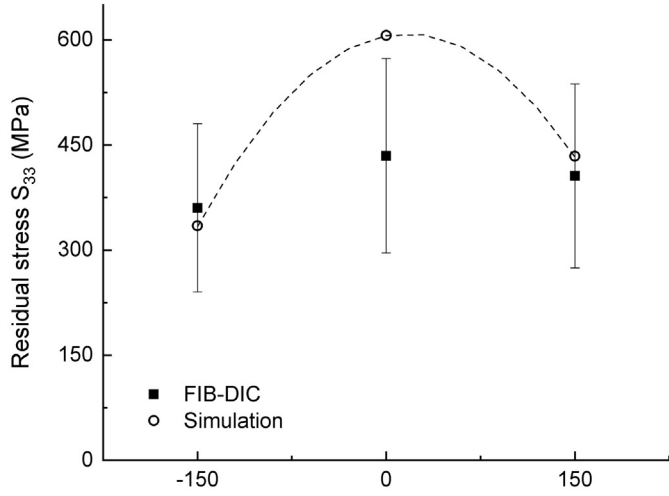
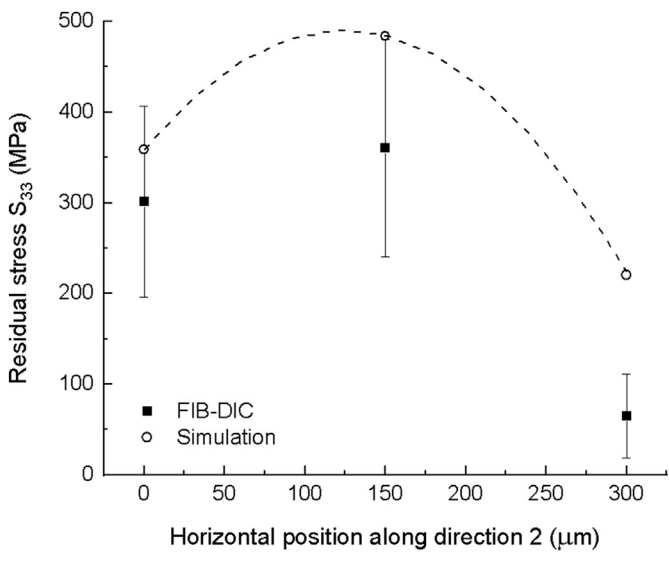


Fig. 12. (a) Area of interest for FIB-DIC residual stress measurement and (b) locations for measurement data point for the FIB-DIC ring cores for LDED-manufactured specimens.



(a)



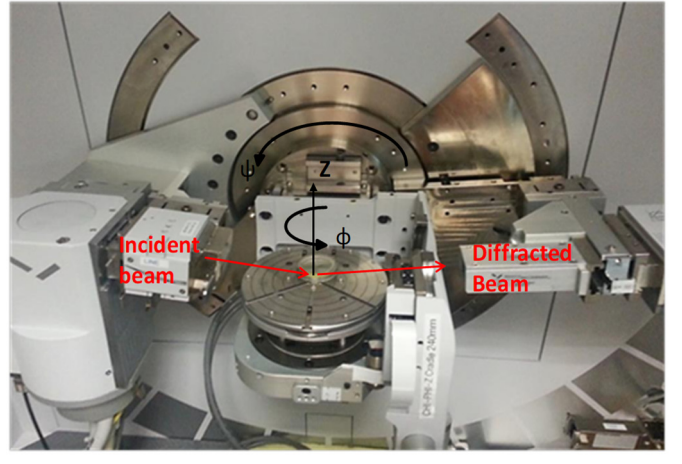
(b)

Fig. 13. Residual stress distribution at the corner of the thin wall along the (a) vertical (direction 1) and (b) horizontal (direction 2) lines for LDED simulation.

lines were selected to compare the results: center, edge, top and bottom. Their indicative locations are illustrated in Fig. 14.

Figs. 15 and 16 show the numerical results for residual stresses before and after cutting in comparison with the experiment. Slitting was performed in the experiment to reveal the middle section for XRD, hence the slitting effect on residual stress development was investigated by adding an additional model change step after the cooling step to remove half of the elements along the cutting lines. We highlight that the additional step redistributes the numerically derived residual stresses within the remaining model and generally reduces stress levels as per presented results.

For the center and edge lines, the residual stress profiles in S_{22} direction for XRD measurements and finite element simulations are plotted in Fig. 15. Both center and edge line show similar trends for numerical and experimental results, that is higher tensile stresses towards the



(a)

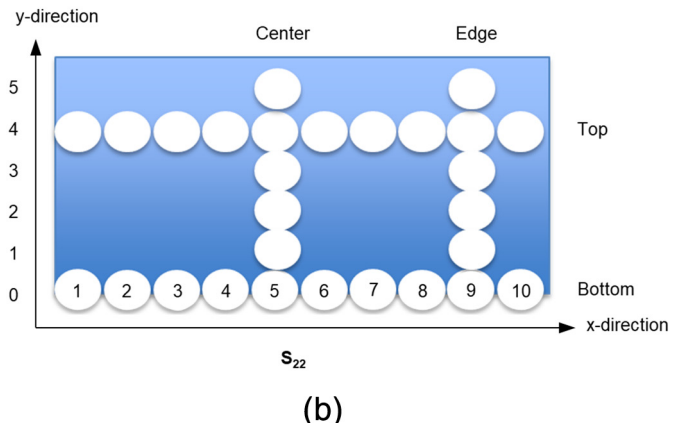
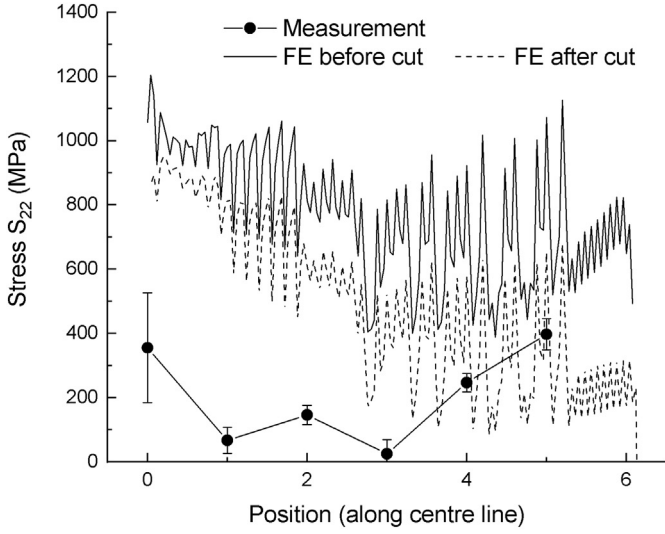


Fig. 14. (a) XRD residual stress measurement set-up and (b) measurement point positions in the LDED thin-wall specimen.

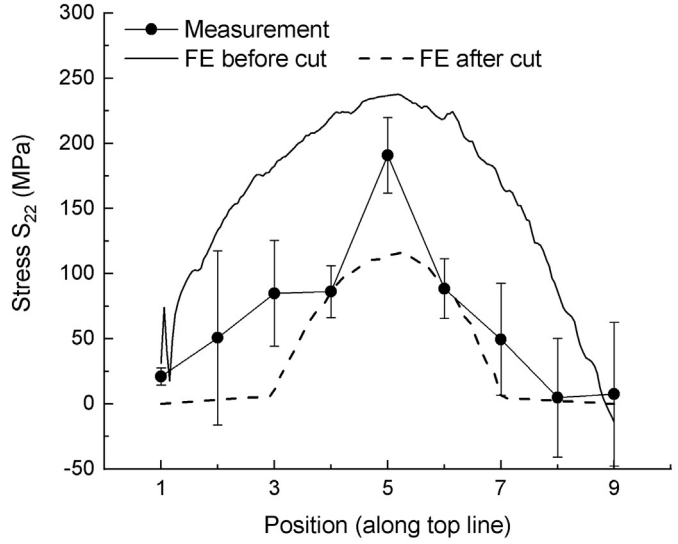
top surface, lesser tensile stresses in the middle section, and high tensile stresses again at the bottom layer where the part meets the baseplate due to the geometry mismatch. Results in the top and bottom horizontal lines depict the same over-estimation of the residual stresses compared to the experimental results before cutting, but it can clearly be seen that the residual stress value drops after simulated EDM slitting and becomes closer to the measurement results. This indicates that ECP and EDM slitting indeed play an important role in the re-distribution of residual stresses in the thin wall component.

Fig. 16 shows higher tensile stresses in the center section of the structure, which drop to zero at the two ends of the top line, as those ends represent the free edge. Simulated residual stress values follow the same trends quite closely when including the cutting process. The bottom cut shows almost constant high tensile stresses in our results and the residual stresses are over-predicted even after cutting. This may be due to lack of strain relaxation mechanism in the plasticity model, which helps to reduce the residual stresses in the bottom layer under the repeated heating and cooling from the layers above. However, consideration of such rate-dependent material behavior could significantly increase the computational time and cause non-convergence issues during iterations.

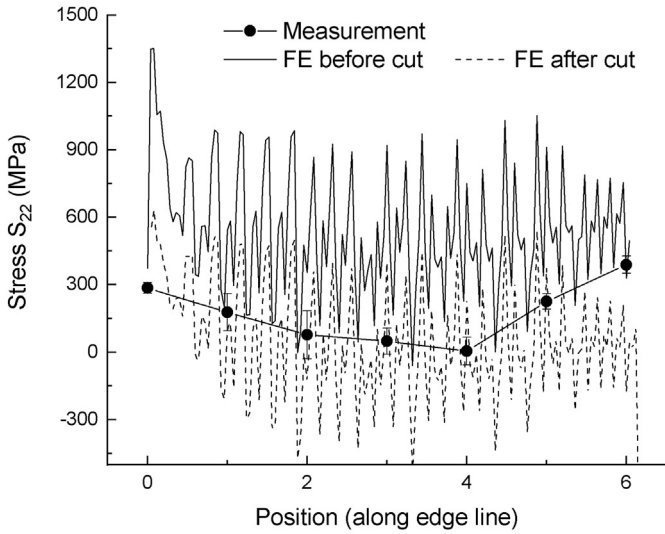
For the top area, the tensile stress in the thin wall build is caused by the constraint from the bottom layer to reduce the volume shrinkage of the build layer from melt to solid state. This is the main cause for vertical cracks which are commonly seen in the top layers. For the middle area, each layer is not only under a tensile stress from the bottom layer, but it is also under a compression stress from the top layer. The two



(a)



(a)

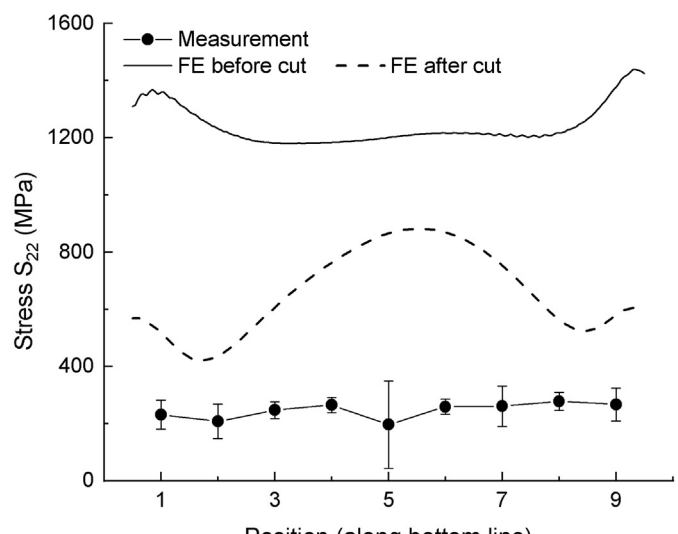


(b)

Fig. 15. Comparison between the residual stress level for the LDED specimen as determined via XRD and finite element simulation before cutting) and after cutting along the (a) center and (b) edge line.

competing factors balance each other and result in a lesser value of tensile stress in the center section. For the bottom area, the high tensile stress is maintained. This is due to the rigid constraint from the base plate. A similar residual stress profile in the scanning direction has also been reported by [36].

Another point to note is, due to the small spot size, the re-melting zone extends into the layer beneath for each added layer. The residual stress in each layer is hence mainly caused by the neighboring bottom layer, and in the meantime, it can only be affected by the adjacent top layer. Therefore, the stress affected zone is highly localized and fluctuating at the frequency of number of layers. From the numerical simulation, we can clearly see such fluctuations in residual stress distributions for the center and edge line cuts as shown in Fig. 15. Similar findings on large stress fluctuations in-between neighboring build layers have also been reported in [36].



(b)

Fig. 16. Comparison between the residual stress level for the LDED specimen as determined via XRD and finite element simulation before cutting and after along the (a) top and (b) bottom line.

Overall, the finite element model generally predicts higher residual stress values than the XRD measurement with the current numerical parameter selection. In this context it should be noted that the stress magnitude is highly sensitive to the selection of the stress-free temperature (here chosen as melt temperature) as well as the plastic properties at high temperatures. The lack of a simulated strain relaxation mechanism may also contribute to the overestimation. Given the long computational time required for the detailed element-by-element model, it is imperative to simplify the simulation process further so that the influence of the material property input on stress development can be studied. This leads to the next section of our work, where the SLM process simulation was carried out with larger time incrementation, hence resulting in significantly shorter simulation time.

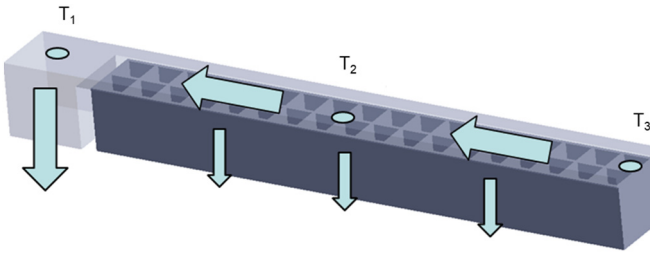


Fig. 17. Temperature analysis locations for FE analysis for SLM cantilever part.

4.3. Distortion prediction in overhanging SLM structure

Fig. 17 shows the main heat transfer path during specimen build for the SLM process for the later stages of the build. Heat is transferred via the solid top plate from location T_3 towards location T_1 and from there to the heated base plate. Location T_2 records the hottest temperature during the build process as the support only offers limited heat transfer capacity towards the build platform compared to the bulk material.

Temperatures along the overhanging part increase away from the solid part on the left as shown in **Fig. 18** to a maximum temperature around location T_2 . The hollow support structure creates a distinctive array of hot spots along the overhang in between the solid support grids and results in much slower cooling of the overhanging part compared to the solid structure on the left. Including the surrounding powder bed in the model results in a higher temperature of the overhanging part, with significant temperature differences of up to 65 °C and 50 °C observed for 0.4 mm and 0.7 mm support thickness, respectively. The temperature gradient along the overhang structure is also significantly larger for the simulation with powder bed. The higher temperatures and gradients are due to the fact that the enclosed powder pockets within the support structure act as a finite heat sink and store heat during the build process. These findings contradict the assumption that conduction to the powder bed may be mimicked by an artificially increased film coefficient [14] or may be neglected [18], especially in cases where thin-walled support structures are utilized or optimized during the build process. The increase in computational time during the heat transfer step is moderate given the increased accuracy of the temperature predictions. Consequently, all subsequent temperature analysis steps were run with a surrounding powder bed. The powder is removed for the subsequent stress analysis as outlined in **Section 3.2**.

When comparing the thickness effect of support structures of 0.4 mm and 0.7 mm on the temperature profiles, the temperatures along the overhanging support (T_2, T_3) increase significantly with a thinner support due to the restricted heat transfer along the support material (**Fig. 19**). In contrast, temperature T_1 is hardly affected by the support thickness as the bulk heat flow along the main build column remains similar. It is noted that the recurring temperature reductions at

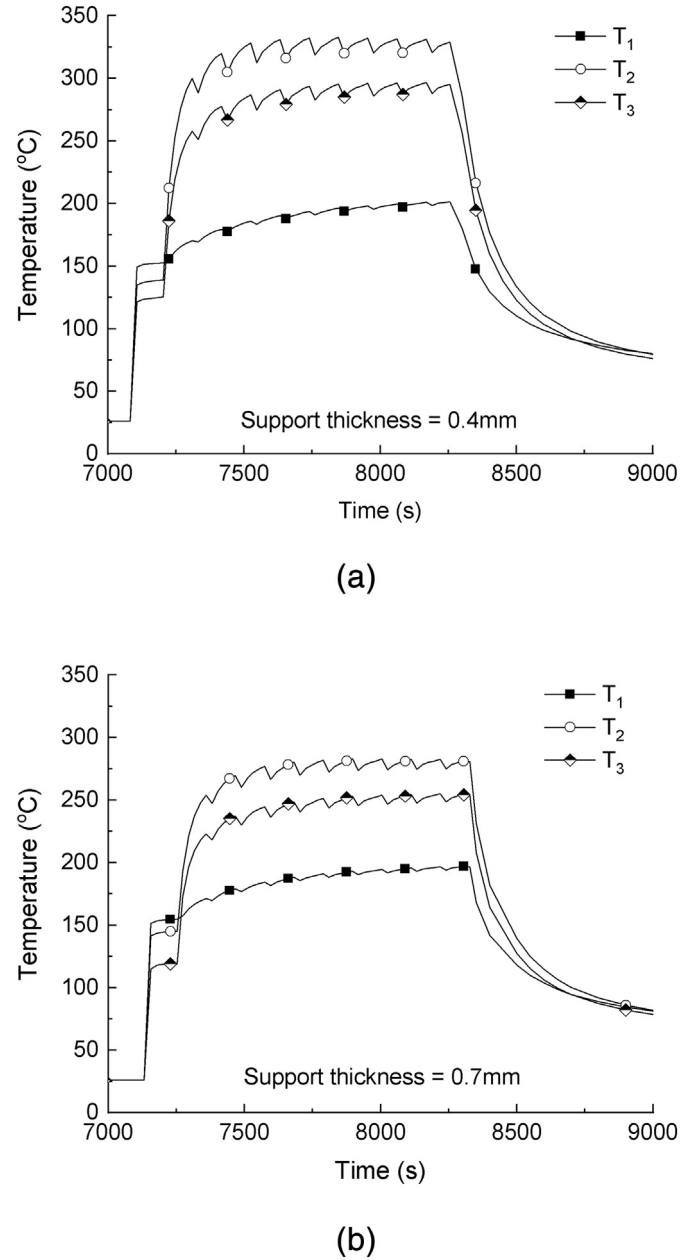


Fig. 19. Local temperatures for SLM cantilever specimens as a function of support structure for (a) 0.4 mm and (b) 0.7 mm thickness. Temperature results are for adiabatic thermal boundary conditions and one time increment per layer (~20–22 s).

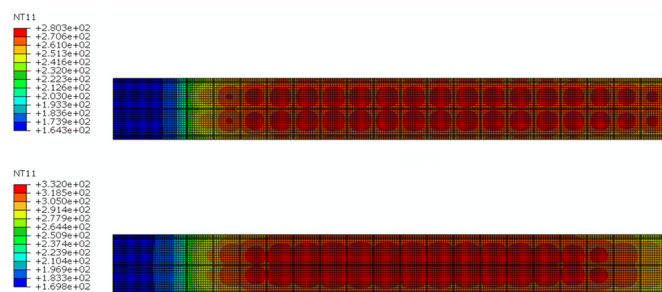
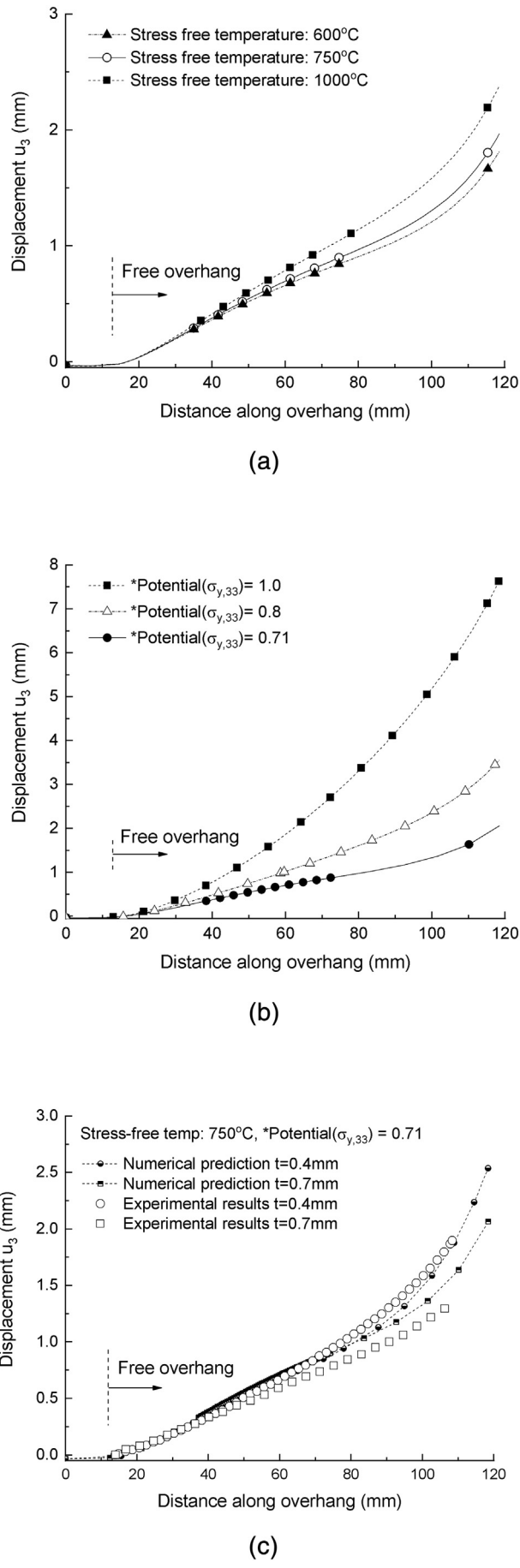


Fig. 18. Temperature contour plot for SLM cantilever part with $t_s = 0.4$ mm at build height of 12.5 mm with (top) and without (bottom) powder bed during thermal analysis. Time incrementation ~22 s (one increment per build layer). A temperature difference of up to 50 °C is observed for this build height.

regular time intervals represent the time of activation of a new element layer [18].

For the residual stress and distortion analysis, a large number of mechanical properties need to be defined. Despite numerous research articles denoted to process simulation, it is noted that the exact parameters for a number of input properties remain unknown. For this reason, the sensitivity to mechanical input parameters is outlined in this paper to provide guidelines for future simulation and experimental studies.

Fig. 20(a) shows the influence of the stress-free temperature. This temperature is difficult to determine experimentally, but is generally expected to be bound by the lower limit of annealing temperature and higher limit of melt temperature. Here, the three values of 600 °C, 750 °C and 1000 °C were investigated. The experimental deflection shape is initially mostly linear and increases nonlinearly towards the end of the overhang. Changes in the stress-free temperature act as scaling factors with the general shape maintained. As expected, a higher

**Table 3**

Influence of input parameters and process set-up on distortion results for SLM cantilever specimens. Results are benchmarked against best simulation fit with orthotropic elastic properties, anisotropic plasticity and a stress free temperature of 750 °C. Surrounding powder bed is considered for the thermal simulation.

Input parameter change	Support thickness [mm]	
	0.4	0.7
No powder bed consideration	+9.3%	+34%
Isotropic stiffness	-7.5%	-8.4%

stress-free temperature increases the maximum deflections as thermal strains are increased.

Unexpectedly, introduction of reduced yield strength in z-direction as per experimental measurements significantly lowered the distortion predictions as per Fig. 20(b). This input parameter is the most influential with regards to the resulting level of distortion. Secondary interactions with the other yield strength components, such as $\sigma_{y,13}$ and $\sigma_{y,23}$ were also observed, but are not further explored here.

The best fit numerical predictions for the deflection traces along the overhang structure are summarized in Fig. 20(c). The agreement between numerical simulation and experimental measurements is generally good for a calibrated best fit stress-free temperature of 750 °C and reduced yield strength in z-direction by almost 30%, although the numerical predictions show a larger amount of curvature in the initial deflection trace of the overhang length up to 80 mm.

It can be seen that the greater difference in temperature gradients along the overhanging structure as shown in Fig. 20 is reflected by an increasing residual stress and hence distortion of the overhanging structure after cutting for thinner support structures of 0.4 mm. The results suggest that increased support thickness results in lower distortion. However, an increase in support structure thickness also results in additional material powder being used in addition to added post-processing cost, hence it is necessary to optimize the thickness of the support structure with these conflicting cost constraints in mind.

Table 3 outlines the effects of several other input parameters on distortion results. The results are again benchmarked against results of best fit as reported in Fig. 20(c). Stress simulations utilizing temperature input without powder bed resulted in larger distortions as expected due to the increased rate of heat loss at the solid boundaries, especially under the overhanging cantilever structure as was shown in Fig. 18. It is interesting to note that the effect is more pronounced for the increased support thickness of 0.7 mm, presumably as the enclosed volume is smaller and surrounded by a thicker (and therefore hotter) support structure. When comparing distortion results with isotropic elastic material behavior to the more accurate orthotropic stiffness input, deflections increase as expected based on the ~10% through-thickness stiffness reduction by a similar amount. Additional simulation runs showed that distortions are also not sensitive to changes in Poisson's ratio values or shear stiffness variations.

Finally, we highlight that the best-fit calibration and sensitivity studies performed here neglect any potential influence of the (1) exact details of the laser path; (2) wire cutting process and (3) influence of residual stresses due to phase transformation. The laser path details are expected to influence the distortion to some extent if significantly finer time increments were chosen to reflect the locally hatched laser source. However, a detailed investigation of studies with reduced time incrementation was found to be unfeasible given the resulting computational time increase. The wire cutting process may influence local stress release due to potential localized heat generation. Phase transformation under rapid cooling conditions and the consideration of the generated residual stresses also requires further investigation. Additionally,

Fig. 20. Deflection of overhanging part as a function of overhang length for SLM cantilever specimen: (a) Influence of stress-free temperature, (b) influence of plastic anisotropy and (c) comparison of prediction against experimental results.

given the highlighted sensitivities to several mechanical input parameters, AM process simulations for 3D structures with detailed experimental verification studies are therefore expected to remain an active research field for future years [37].

5. Conclusions

In the present study, we have evaluated current ABAQUS AM module capabilities to take on the challenges of full process simulation of complex metal components. Our studies show that the new modelling framework allows for quantitative investigation of effects such as processing parameter variation, structural geometry constraints, as well as influence of building plate and surrounding powder. The Abaqus AM module allows users to specify process-dependent information (such as tool path, build environment, power input) as input in space and time to create event series within a common numerical framework. Such approaches automate laser movement and element activation independent of mesh geometry and element type, hence greatly reducing the data I/O and computational time and making the lengthy and repetitive AM simulation work manageable. The additive manufacturing process and the desired experimental validation methodology determine the most appropriate modelling approach in terms of mesh density, element activation approach, and heat input and time increment resolution.

The two investigated numerical approaches utilizing (1) fine mesh approaches with Goldak heating resolution and (2) coarser mesh solutions with node-based distributed heat flux simplification result in good agreement for local temperature predictions for similar time step resolution, with significant computational time savings achieved for the latter method due to the reduced number of elements. Computational time can be further reduced by increasing the time incrementation during the thermal analysis. While this affects the local temperature profile peaks and hence predicted cooling rates, this simplification is generally considered to have a limited effect on the overall distortions of complex 3D geometries during the printing process.

The conducted process simulations allowed us to study the effects material property anisotropy with regard to residual stress and distortion predictions, leading to unexpected sensitivities in numerical results. It is highlighted that experimental data input for plastic anisotropy remains an on-going field of research for as-built properties. It is concluded that further research work needs to focus on more accurate measurements of these critical material properties at elevated temperature to improve the fidelity of process simulations.

Funding

This work is supported by the Singapore Agency for Science, Technology and Research (A*STAR) and the Science and Engineering Research Council (SERC) project grant number 142 68 00088 (SIMTech-led Additive Manufacturing Center projects - Work Packages 3 and 4).

CRediT authorship contribution statement

Xu Song: Conceptualization, Methodology, Software, Investigation, Writing – original draft. **Stefanie Feih:** Conceptualization, Methodology, Software, Investigation, Writing – original draft. **Wei Zhai:** Formal analysis, Validation, Writing – review & editing. **Chen-Nan Sun:** Validation. **Feng Li:** Resources, Funding acquisition, Project administration. **Raj Maiti:** Resources, Funding acquisition, Project administration. **Jun Wei:** Resources. **Yangzhan Yang:** Software. **Victor Oancea:** Software, Supervision. **Leon Romano Brandt:** Validation. **Alexander M. Korsunsky:** Validation, Supervision.

Declaration of competing interest

The authors declare that they have no known competing financial interests or personal relationships that could have appeared to influence the work reported in this paper.

References

- [1] International Organization for Standardization, Additive Manufacturing — General Principles — Overview of Process Categories and Feedstock, ISO/ASTM International Standard, 2015 (17296-2:2015(E)).
- [2] T. Gatsos, K.A. Elsayed, Y. Zhai, D.A. Lados, Review on computational modeling of process-microstructure-property relationships in metal additive manufacturing, *J. Metals* 72 (1) (2020) 403–419.
- [3] T. DebRoy, H.L. Wei, J.S. Zuback, T. Mukherjee, J.W. Elmer, J.O. Milewski, A.M. Beese, A. Wilson-Heid, A. Ded, W. Zhang, Additive manufacturing of metallic components – process, structure and properties, *Prog. Mater. Sci.* 92 (2018) 112–224.
- [4] P. Mercelis, J.-P. Kruth, Residual stresses in selective laser sintering and selective laser melting, *Rapid Prototyp. J.* 12 (5) (2006) 254–265.
- [5] M. Shiomil, K. Osakadal, K. Nakamura, T. Yamashita, F. Abe, Residual stress within metallic model made by selective laser melting process, *CIRP Ann.* 53 (1) (2004) 195–198.
- [6] J.P. Oliveira, T.G. Santos, R.M. Miranda, Revisiting fundamental welding concepts to improve additive manufacturing: from theory to practice, *Prog. Mater. Sci.* 107 (2020), 100590.
- [7] P.J. Withers, H.K.D.H. Bhadeshia, Residual stress. Part 1 – measurement techniques, *Mater. Sci. Technol.* 17 (4) (2001) 355–365.
- [8] X. Song, M. Xie, F. Hofmann, T. Illston, T. Connolley, C. Reinhard, R.C. Atwood, L. Connor, M. Drakopoulos, L. Frampton, A.M. Korsunsky, Residual stresses and microstructure in powder bed direct laser deposition (PB-DLD) samples, *Int. J. Mater. Form.* 8 (2) (2015) 245–254.
- [9] A.S. Wu, D.W. Brown, M. Kumar, G.F. Gallegos, W.E. King, An experimental investigation into additive manufacturing-induced residual stresses in 316L stainless steel, *Metall. Mater. Trans. A* 45 (13) (2014) 6260–6270.
- [10] F. Schmeiser, E. Krohmer, N. Schell, E. Uhlmann, W. Reimers, Experimental observation of stress formation during selective laser melting using in-situ X-ray diffraction, *Addit. Manuf.* 32 (2020), 101028.
- [11] L. Parry, I.A. Ashcroft, R.D. Wildman, Understanding the effect of laser scan strategy on residual stress in selective laser melting through thermo-mechanical simulation, *Addit. Manuf.* 12 (A) (2016) 1–15.
- [12] Q. Zhang, J. Xie, Z. Gao, T. London, D. Griffiths, V. Oancea, A metallurgical phase transformation framework applied to SLM additive manufacturing processes, *Mater. Des.* 166 (2019), 107618..
- [13] Q. Zhang, J. Xie, T. London, D. Griffiths, I. Bhamji, V. Oancea, Estimates of the mechanical properties of laser powder bed fusion Ti-6Al-4V parts using finite element models, *Mater. Des.* 169 (2019), 107678..
- [14] C. Li, E.R. Denlinger, M.F. Gouge, J.E. Irwin, P. Michaleris, Numerical verification of an Octree mesh coarsening strategy for simulating additive manufacturing processes, *Addit. Manuf.* 30 (2019), 100903..
- [15] A.J. Dunbar, E.R. Denlinger, M.F. Gouge, P. Michaleris, Experimental validation of finite element methodology for laser powder bed fusion deformation, *Addit. Manuf.* 12 (2016) 108–120.
- [16] S.A. Khairallah, A. Anderson, Mesoscopic simulation model of selective laser melting of stainless steel powder, *J. Mater. Process. Technol.* 214 (11) (2014) 2627–2636.
- [17] C. Li, J.F. Liu, X.Y. Fang, Y.B. Guo, Efficient predictive model of part distortion and residual stress in selective laser melting, *Addit. Manuf.* 17 (2017) 157–168.
- [18] Y. Yang, M. Allen, T. London, V. Oancea, Residual strain predictions for a powder bed fusion Inconel 625 single cantilever part, *Integrating Mater. Manuf. Innov.* 8 (2019) 294–304.
- [19] Abaqus User's Manual, <https://www.3ds.com/products-services/simulia/support/documentation/> 2018.
- [20] X. Song, Residual stress modeling and measurement of material addition thin wall buildups, Rolls Royce Industry Report, Singapore Institute of Manufacturing Technology, A*STAR, 2017.
- [21] B. Zhang, X. Lee, J. Bai, J. Guo, P. Wang, C.N. Sun, M.L. Nai, G. Qi, J. Wei, Study of selective laser melting (SLM) Inconel 718 part surface improvement by electrochemical polishing, *Mater. Des.* 116 (2017) 531–537.
- [22] M.E. Fitzpatrick, A.T. Fry, P. Holdway, F.A. Kandil, J. Shackleton, L. Suominen, Determination of Residual Stresses by X-ray Diffraction, National Physical Laboratory, Teddington, UK, 2005.
- [23] EOS Nickel Alloy IN718 Material Data Sheet, , EOS GmbH Germany, 2014 www.eos.info.
- [24] J. Goldak, A. Chakravarti, M. Bibby, A new finite element model for welding heat sources, *Metall. Trans. B* 15 (1984) 299–305.
- [25] L. Han, K.M. Phatak, F.W. Liou, Modeling of laser cladding with powder injection, *Metall. Mater. Trans. B Process Metall. Mater. Process. Sci.* 35 (2004) 1139–1150.
- [26] S. Raghavan, B. Zhang, P. Wang, C.N. Sun, M.L.S. Nai, T. Li, J. Wei, Effect of different heat treatment on the microstructure and mechanical properties in selective laser melted Inconel 718 alloy, *Mater. Manuf. Process.* 32 (14) (2016) 1–8.
- [27] P.E. Aba-Perea, T. Pirlin, P.J. Withers, J. Kelleher, S. Kabra, M. Preuss, Determination of the high temperature elastic properties and diffraction elastic constants of Ni-base superalloys, *Mater. Des.* 89 (2017) 856–863.
- [28] Y. Zhang, T.T. Zuo, Z. Tang, M.C. Gao, K.A. Dahmen, P.K. Liaw, Z.P. Lu, Microstructures and properties of high-entropy alloys, *Prog. Mater. Sci.* 61 (2014) 1–93.

- [29] S. Yagi, D. Kunii, Studies of effective thermal conductivities in packed beds, *AIChE J.* 3 (3) (1957) 373–381.
- [30] M. Jamshidinia, F. Kong, R. Kovacevic, Numerical modeling of heat distribution in the Electron beam melting of Ti-6Al-4V, *J. Manuf. Sci. Eng.* 135 (6) (2013), 061010..
- [31] S. Feih, C.N. Sun, B. Zhang, Q.L. Lo, C. Chin, J. Wei, Influence of Surrounding Powder Bed and Build Platform on Thermal Cooling Characteristics in 3D Printed Parts Via Selective Laser Melting, *Science in the Age of Experience*, Chicago, USA, 2017.
- [32] A.M. Korsunsky, M. Sebastiani, E. Bemporad, Residual stress evaluation at the micrometer scale: analysis of thin coatings by FIB milling and digital image correlation, *Surf. Coat. Technol.* 205 (2010) 2393–2403.
- [33] M. Sebastiani, C. Eberl, E. Bemporad, A.M. Korsunsky, W.D. Nix, F. Carassiti, Focused ion beam four-slot milling for Poisson's ratio and residual stress evaluation at the micron scale, *Surf. Coat. Technol.* 251 (2014) 151–161.
- [34] X. Song, Z.Q. Zhang, S. Narayanaswamy, Y.Z. Huang, M. Zarinejad, Numerical and experimental study on the residual stresses in the nitrided steel, *J. Mater. Eng. Perform.* 25 (9) (2016) 4036–4045.
- [35] X. Song, J. Everaerts, W. Zhai, H. Zheng, W.Y. Tan, W. Sun, F. Li, I. Marinescu, E.J. Liu, A.M. Korsunsky, Residual stresses in single particle splat of metal cold spray process – numerical simulation and direct measurement, *Mater. Lett.* 230 (2018) 152–156.
- [36] T. Mukherjee, W. Zhang, T. DebRoy, An improved prediction of residual stresses and distortion in additive manufacturing, *Comput. Mater. Sci.* 126 (2017) 360–372.
- [37] L. Bertini, F. Buchi, F. Frendo, M. Moda, B.D. Monelli, Residual stress prediction in selective laser melting, *Int. J. Adv. Manuf. Technol.* 105 (2019) 609–636.